

Polarization Control with Plasmonic Antenna Tips: A Universal Approach to Optical Nanocrystallography and Vector-Field Imaging

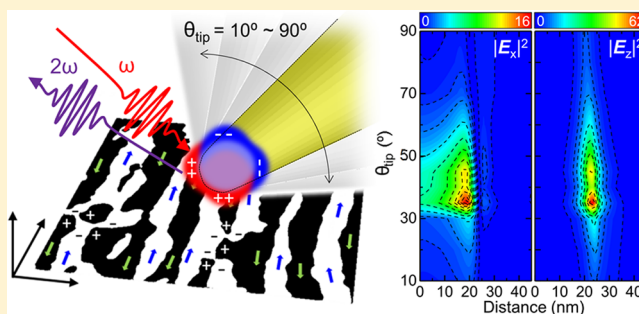
Kyoung-Duck Park¹ and Markus B. Raschke^{1*}

Department of Physics, Department of Chemistry, JILA, and Center for Experiments on Quantum Materials, University of Colorado, Boulder, Colorado 80309, United States

Supporting Information

ABSTRACT: Controlling the propagation and polarization vectors in linear and nonlinear optical spectroscopy enables us to probe the anisotropy of optical responses providing structural symmetry selective contrast in optical imaging. Here, we present a novel tilted antenna-tip approach to control the optical vector-field by breaking the axial symmetry of the nanoprobe in tip-enhanced near-field microscopy. This gives rise to a localized plasmonic antenna effect with significantly enhanced optical field vectors with control of both in-plane and out-of-plane components. We use the resulting vector-field specificity in the symmetry selective nonlinear optical response of second-harmonic generation (SHG) for a generalized approach to optical nanocrystallography and imaging. In tip-enhanced SHG imaging of monolayer MoS₂ films and single-crystalline ferroelectric YMnO₃, we reveal nanocrystallographic details of domain boundaries and domain topology with enhanced sensitivity and nanoscale spatial resolution. The approach is applicable to any anisotropic linear and nonlinear optical response and enables the optical nanocrystallographic imaging of molecular or quantum materials.

KEYWORDS: Tip-enhanced second-harmonic generation, vector-field control, optical nanocrystallography, MoS₂, YMnO₃, domain boundary



Symmetry selective optical imaging of, e.g., crystallinity, molecular orientation, and static or dynamic ferroic order and polarization is desirable, yet as of today, access to these internal material properties on the micro- to nanoscale has not been provided in optical microscopy in a systematic way. Molecular vibrations, phonons, excitons, and spins in their interaction with light give rise to an anisotropic linear and nonlinear optical response. This optical response is sensitive to the direction of the wave vector and the polarization of the optical driving fields and correlated with the structural symmetries of the material.^{1,2} In reflection or transmission measurements of far-field optical imaging and spectroscopy, the transverse projection of the optical field as determined by the laws of linear and nonlinear reflection, and refraction gives access to the optical selection rules associated with the materials symmetries^{3–6} yet with limited degrees of freedom constrained by the wave vector conservation in far-field optics.

In contrast, wave vector conservation is lifted in near-field scattering depending on the structure and orientation of the nano-objects as scattering elements. In combination with near-field imaging based on tip scattering, in scanning near-field microscopy and spectroscopy, one can increase the degrees of freedom with the choice of incident and detected wave vector, independent from the active control of the local polarization through an engineered antenna-tip response. However, to date, most scanning near-field microscopy studies have focused on a

surface normal-oriented antenna-tip in tip-enhanced near-field microscopy^{7–9} based on the hypothesis of maximum field enhancement in this configuration.

While this conventional tip geometry is useful for selectively detecting an out-of-plane (perpendicular with respect to the sample plane) polarized response, it reduces the detection sensitivity for in-plane (parallel with respect to the sample plane) polarization. Artificial tip engineering for enhanced in-plane sensitivity limits spatial resolution and universal applicability, requiring a complex tip-fabrication process, or some combination of thereof.^{10–13} These limitations in measuring the in-plane optical response restrict the range of optical techniques and sample systems. Specifically, predominantly two-dimensional (2D) quantum systems, such as graphene,^{14–16} transition-metal dichalcogenides (TMDs),^{17–19} epitaxial thin films,²⁰ and important classes of transition metal oxides of layered materials,²¹ all with dominant in-plane excitations, are difficult to probe. Therefore, to broadly extend the range of near-field microscopy application to the characterization of nanophotonic structures and metasurfaces,²² or optical nanocrystallography and nanoimaging of anisotropic

Received: January 9, 2018

Revised: March 3, 2018

Published: March 23, 2018

samples,^{23,24} a new approach with extended antenna-tip vector-field control is desirable.^{25,26}

Here, we demonstrate a generalizable approach to controlling the excitation and detection polarizability for both in-plane and out-of-plane vector-fields in nanoimaging with enhanced sensitivity and without a loss of spatial resolution. We break the axial symmetry of a conventional metal tip by varying its tilt angle with respect to the sample surface. By varying the tilt angle, we control the ratio of in-plane and out-of-plane polarization. This oblique angle of the tip axis gives rise to significant field enhancement in both polarization directions based on localized surface plasmon resonances (LSPR).^{27–30}

Second-harmonic generation (SHG) microscopy provides structural insight into materials through the nonlinear optical response, such as crystal symmetry, orientation, defect states, stacking angle, and the number of layers.^{31–33} We take advantage of the near-field polarization control in both the excitation and the detection fields in symmetry selective tip-enhanced SHG imaging, as an example, applied to different quantum materials. To quantify the enhanced sensitivity of the tilted tip and to image nanocrystallographic properties, we perform grain boundary (GB) mapping of monolayer MoS₂ as a model system of layered 2D materials. This is achieved by the reduced nonlinear optical susceptibility and modified selection rule at the GBs. In addition, on single crystal YMnO₃, by mapping both in-plane and out-of-plane nonlinear optical susceptibility $\chi_{ijk}^{(2)}$ components,^{34,35} we obtain ferroelectric domain nanoimaging facilitated by the local phase-sensitive detection³⁵ with enhanced SHG sensitivity. These experimental results demonstrate a substantial gain in image content from a simple yet effective modification to the conventional tip-enhanced imaging approach. The approach is expected to greatly enhance the sensitivity of optical nanospectroscopy in any linear and nonlinear optical modality and then extends the application space of optical nanoimaging to a wider range of materials.

Experimental Section. The experiment is based on tip-enhanced spectroscopy,¹⁷ with side illumination of the electrochemically etched Au tip manipulated in a shear-force atomic force microscope (AFM), as shown schematically in Figure 1a. The sample surface can be tilted by variable angle with respect to the tip axis from 0° to 90°. Excitation light provided from a Ti/sapphire oscillator (FemtoSource Synergy, Femtolasers Inc., with $\tau \approx 11$ fs pulse duration, center wavelength of 800 nm, 78 MHz repetition rate, and <2 mW of power) is focused onto the tip–sample junction using an objective lens (NA = 0.8, WD = 4 mm) with polarization and dispersion control. The back-scattered SHG signal is polarization selected and detected using a spectrometer (SpectraPro 500i, Princeton Instruments, $f = 500$ mm) with a charge-coupled device (CCD) camera (ProEM+: 1600 eXcelon3, Princeton Instruments).

In excitation and detection, we define *p* and *s* polarization as light polarized in parallel and perpendicular directions, respectively, with respect to the plane formed by *k*-vector and tip axis. In $p_{in}p_{out}$ (*p*-polarized excitation and *p*-polarized detection) configuration, the broken axial symmetry gives rise to a tip-SHG response with expected power (Figure 1b) and polarization (Figure 1c) dependence of the SHG response. In SHG nanoimaging, the intrinsic tip-SHG response can be discriminated from the tip–sample coupled response through polarization and tip–sample distance-dependent measurements.

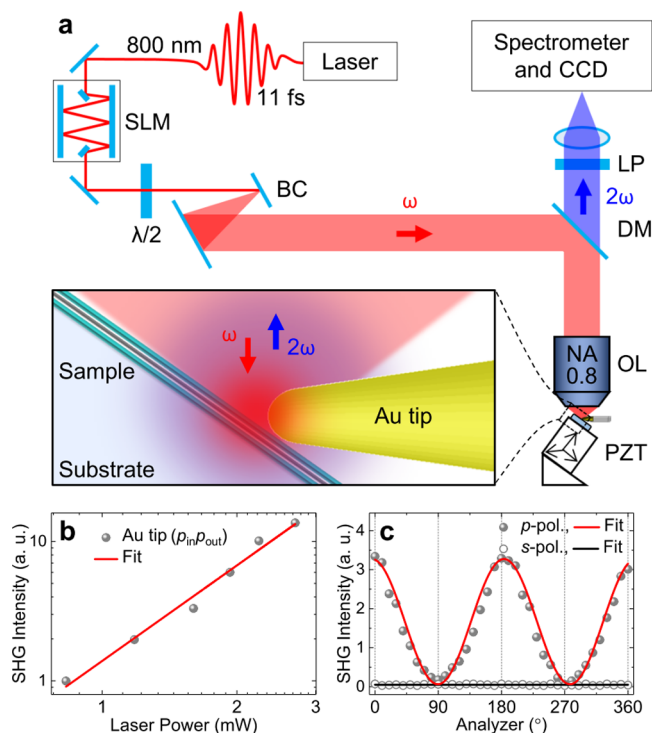


Figure 1. (a) Schematic of tip-enhanced SHG nanospectroscopy and nanoimaging. SLM, spatial light modulator; $\lambda/2$, half-wave plate; BC, beam collimator; DM, dichroic mirror; OL, objective lens; LP, linear polarizer (analyzer). (b) Log plot of the power dependence of near-field SHG intensity of Au tip in $p_{in}p_{out}$ configuration. (c) Polarization dependence of SHG intensity of Au tip for *p*- (red) and *s*- (black) polarized excitation.

Note that a tilted tip geometry has been used previously in several cases of top-illumination tip-enhanced Raman spectroscopy (TERS).^{36,37} However, this only served the purpose of ease of tip illumination without any vector-field control.

Results and Discussion. Vector-Field Control with Plasmonic Antenna Tip. To characterize the local optical field enhancement with respect to the tilt angle of the Au tip, we calculate the expected optical field distribution using finite-difference time-domain (FDTD) simulations (Lumerical Solutions, Inc.) for our experimental conditions. Panels a and e of Figure 2 show the in-plane optical field maps ($|E_x|^2$ and $\text{Re}[E_x]$) for surface-normal tip orientation ($\theta_{tip} = 90^\circ$) with an SiO₂ substrate, with excitation (800 nm) polarization perpendicular with respect to the tip axis. A weak E_x field confinement at the apex is seen resulting from the transverse local antenna mode.^{27,28} To achieve an efficient local plasmon antenna effect, we model the tilted tip with excitation polarization parallel with respect to the tip axis. Panels b and f of Figure 2 show calculated $|E_x|^2$ and $\text{Re}[E_x]$ distributions for the 35° tilted tip orientation ($\theta_{tip} = 35^\circ$), exhibiting in-plane optical field intensity approximately 6 times stronger than that of the sample-surface-normal orientation (Figure 2a). Notably, for this tilt angle, the out-of-plane vector-field is also significantly enhanced, as seen in panels c, d, g, and h of Figure 2.

To characterize a systematic change of vector-field enhancement, we calculate the in-plane and out-of-plane optical field intensity with respect to tilt angle. Panels a and b of Figure 3 show simulated vector-field intensity profiles for $|E_x|^2$ and $|E_z|^2$ at the sample plane (the distance between tip and sample is set

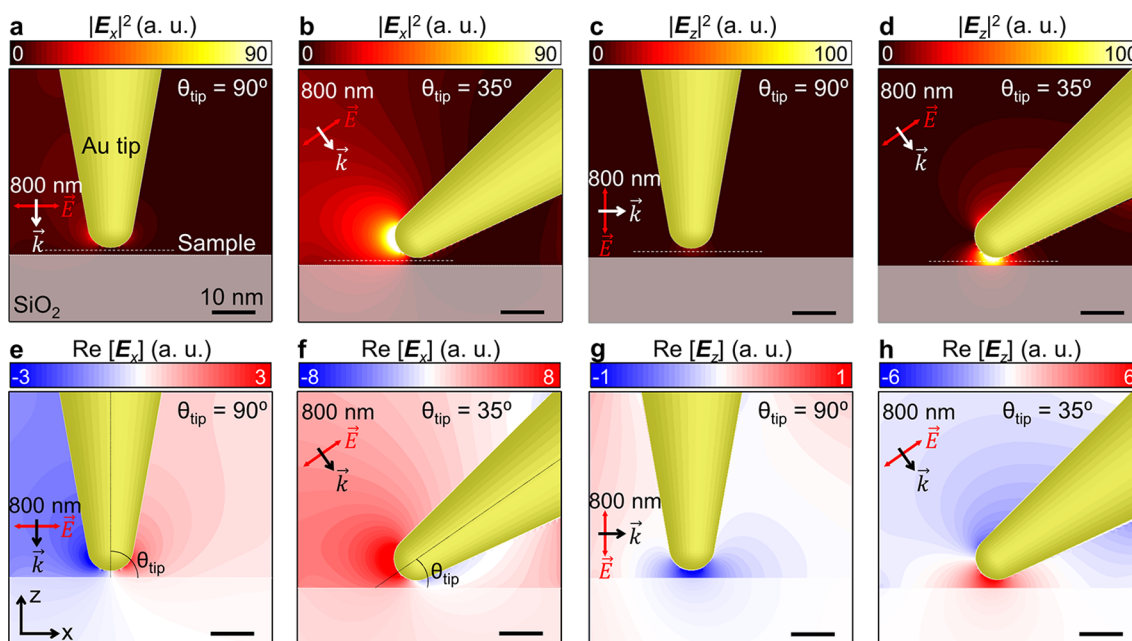


Figure 2. Simulated optical field distributions for surface-normal tip orientation ($\theta_{\text{tip}} = 90^\circ$, in-plane: (a) $|E_x|^2$ and (e) $\text{Re}[E_x]$; out-of-plane: (c) $|E_z|^2$ and (g) $\text{Re}[E_z]$) and for optimal tilted tip orientation ($\theta_{\text{tip}} = 35^\circ$, in-plane: (b) $|E_x|^2$ and (f) $\text{Re}[E_x]$; out-of-plane: (d) $|E_z|^2$ and (h) $\text{Re}[E_z]$).

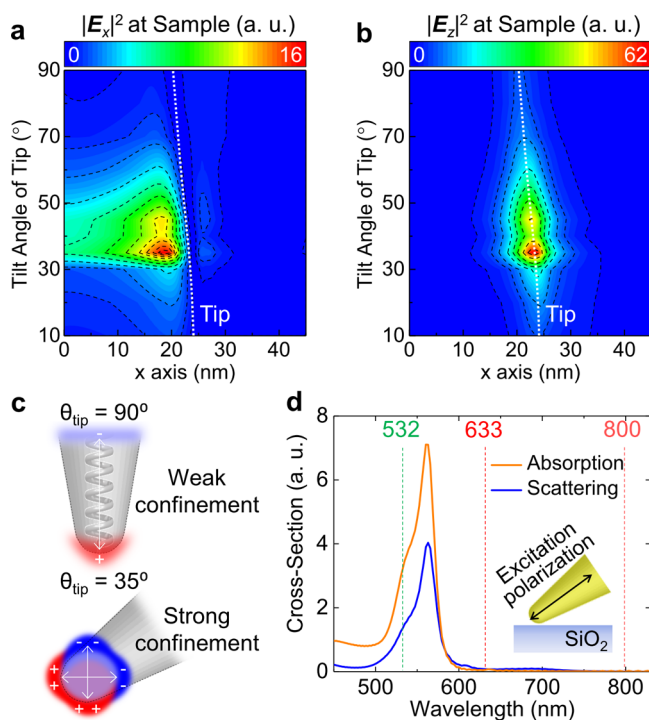


Figure 3. Simulated (a) in-plane $|E_x|^2$ and (b) out-of-plane $|E_z|^2$ optical field intensity profiles at the sample plane with respect to the tilt angle of the tip (θ_{tip}). (c) Schematic showing spatial confinement of free electron oscillation for conventional vertically oriented tips (top, $\theta_{\text{tip}} = 90^\circ$) and tilted tips (bottom, $\theta_{\text{tip}} = 35^\circ$). (d) FDTD simulations of the absorption and scattering cross-sections for the tilted Au tip ($\theta_{\text{tip}} = 35^\circ$) with SiO_2 substrate.

to 0.5 nm; see Figures S1–S9 for the full data set of the tilt-angle-dependent $|E_x|^2$ and $|E_z|^2$). For the small ($10^\circ \leq \theta_{\text{tip}} \leq 30^\circ$) and large ($60^\circ \leq \theta_{\text{tip}} \leq 90^\circ$) tilt angles, the field confinement is not significantly enhanced compared to conventional tip orientation ($\theta_{\text{tip}} = 90^\circ$) due to the over-

damped resonance of the electrons oscillation in a semi-infinite tip structure. In this case, the Au tip cannot sustain strong antenna-like in-plane and out-of-plane surface plasmon polaritons (SPPs).²⁸ However, the field confinement is significantly enhanced for the tilt angles between 30° and 60° because geometric confinement gives rise to an appreciable LSPR effect, as illustrated in Figure 3c. Note that the Au tip with the SiO_2 substrate provides for larger vector-field enhancement than the free-standing tip because the SiO_2 substrate gives rise to an induced dipole coupling between the tip and sample (see Figures S1–S9 discussing the substrate effect).³⁸ It should be noted that the polarization of optical near-field at the tilted tip apex can be further controlled by, e.g., radially polarized light for enhanced $|E_z|$ or azimuthally polarized light for enhanced $|E_x|$.²⁶

Figure 3d shows calculated absorption and scattering cross-section spectra for the tilted Au tip ($\theta_{\text{tip}} = 35^\circ$) near the SiO_2 substrate. The LSPR of the tilted tip is at ~ 550 nm near the interband transition of gold (2.4 eV) and has a modified spectral shape and line width due to the elongated structure and correspondingly modified radiative damping.³⁹ Table 1 shows comparisons of the resulting in-plane and out-of-plane vector-field intensity enhancement for conventional tips ($\theta_{\text{tip}} = 90^\circ$) and tilted tips ($\theta_{\text{tip}} = 35^\circ$) for selected on- and off-

Table 1. Comparison of In-Plane and Out-of-Plane Optical-Field Intensity Enhancement for Conventional ($\theta_{\text{tip}} = 90^\circ$) and Tilted ($\theta_{\text{tip}} = 35^\circ$) Tip for Selected Excitation Wavelengths, Exhibiting Larger Field Enhancement of the Tilted Tip at the Resonance Excitation for Both $|E_x|^2$ and $|E_z|^2$

	$ E_x/E_0 ^2$ (in-plane)		$ E_z/E_0 ^2$ (out-of-plane)	
	$\theta_{\text{tip}} = 90^\circ$	$\theta_{\text{tip}} = 35^\circ$	$\theta_{\text{tip}} = 90^\circ$	$\theta_{\text{tip}} = 35^\circ$
$\lambda_{\text{exc}} = 532$ nm	28	290	40	630
$\lambda_{\text{exc}} = 633$ nm	23	180	42	250
$\lambda_{\text{exc}} = 800$ nm	16	90	25	100

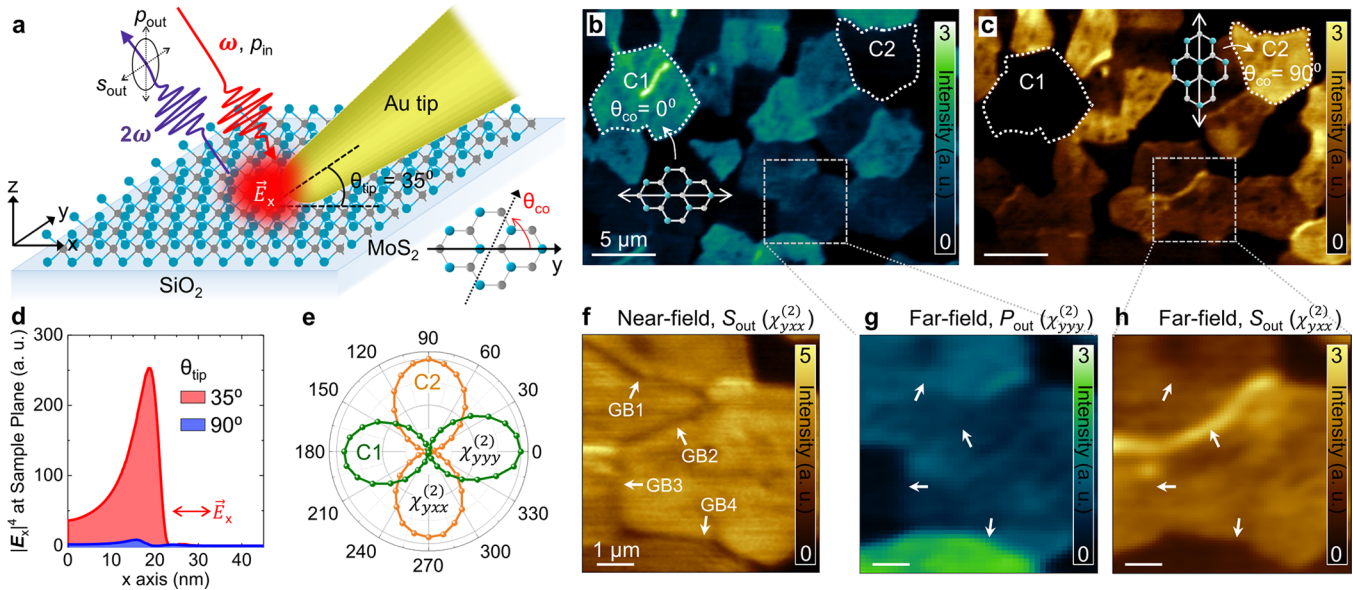


Figure 4. (a) Schematic of tip-enhanced SHG nanocrystallographic imaging of monolayer MoS₂ films on a SiO₂ substrate. Far-field SHG images measured in (b) $p_{in}p_{out}$ and (c) $p_{in}s_{out}$ configurations. (d) Simulated $|E_x|^{4^t}$ profile at sample plane for tilted ($\theta_{tip} = 35^\circ$) and conventional ($\theta_{tip} = 90^\circ$) tip orientations. (e) Far-field SHG polarization dependence of crystals C1 and C2 in panels b and c. (f) Tip-enhanced SHG nanocrystallographic image of the same area measured in the $p_{in}s_{out}$ configuration. (g, h) Magnified far-field SHG images of the small area in panels b and c.

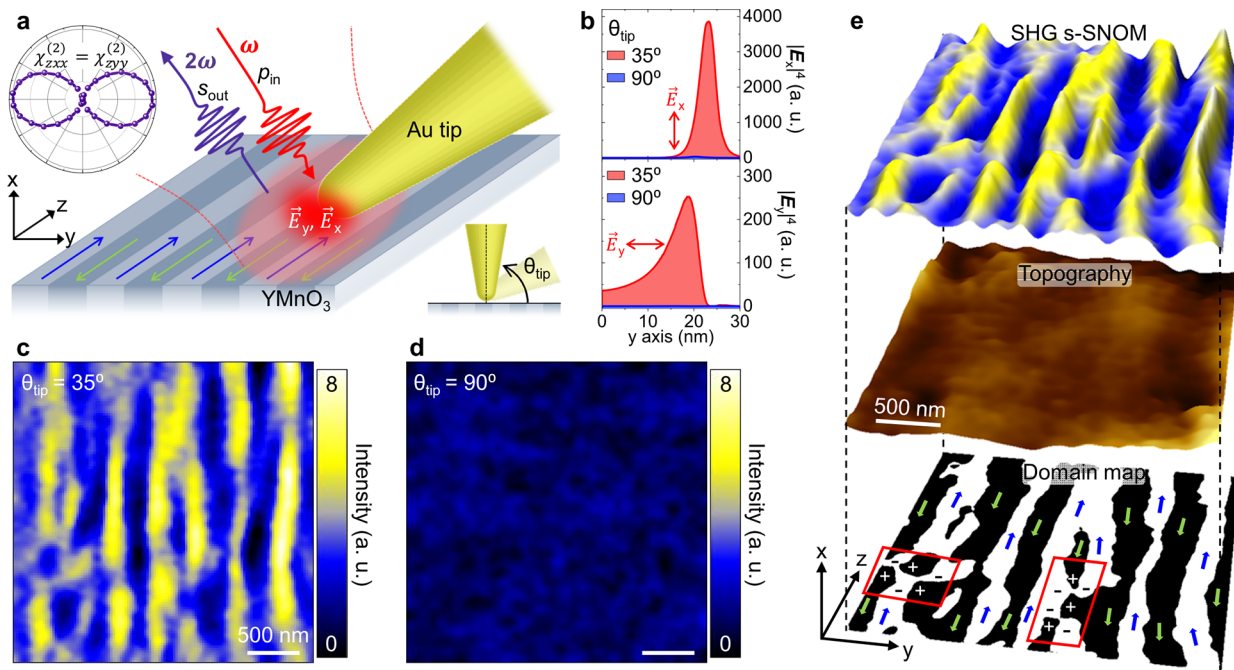


Figure 5. (a) Schematic of tip-enhanced SHG nanocrystallographic imaging of single-crystalline x -cut YMnO₃. (b) Simulated $|E_x|^{4^t}$ (out-of-plane) and $|E_y|^{4^t}$ (in-plane) profiles at sample plane for tilted ($\theta_{tip} = 35^\circ$) and conventional ($\theta_{tip} = 90^\circ$) tip orientations. Tip-enhanced SHG nanocrystallographic image measured by tilted (panel c, $\theta_{tip} = 35^\circ$) and conventional (panel d, $\theta_{tip} = 90^\circ$) tip. (e) The 3D representation of SHG nanocrystallographic image and topography together with the corresponding ferroelectric domain map.

resonance excitation wavelengths. As can be seen, the tilted tip results in a much larger optical field enhancement for both $|E_x|/E_0|^2$ ($I_\omega^{35^\circ}/I_\omega^{90^\circ} \approx 6-10$) and $|E_z|/E_0|^2$ ($I_\omega^{35^\circ}/I_\omega^{90^\circ} \approx 4-16$) for all wavelengths, with the largest effect on resonance. Based on these results, we confirm a strongly localized plasmon resonance of the tilted tip in contrast to a reduced resonance effect for surface-normal tip orientation.

Nonlinear Optical Nanocrystallography and Nanoimaging. As illustrated in Figure 4a, we perform tip-enhanced nano-

SHG imaging with the 35° tilted antenna tip for single-layer MoS₂ films grown on a SiO₂/Si substrate.⁶ This was used as a model system of a $\bar{6}m2$ point group possessing pure in-plane $\chi_{ijk}^{(2)}$ tensor elements.^{31,40,41}

For comparison, we first perform conventional far-field imaging to determine the crystal orientation angle (θ_{co}) and GB of the TMD crystals.^{6,42} Panels b and c of Figure 4 show far-field SHG images with polarization selections of $p_{in}p_{out}$ and $p_{in}s_{out}$ respectively. From the nonvanishing $\chi_{ijk}^{(2)}$ tensor elements

and excitation condition, the induced second-order polarization for crystals with $\theta_{\text{co}} = 0^\circ$ (C1 of Figure 4b,c) is given by $\mathbf{P}_y(2\omega) = 2\epsilon_0\chi_{yyy}^{(2)}\mathbf{E}_y(\omega)^2$, where $\mathbf{E}_{i=x,y,z}(\omega)$ are the electric field components at the laser frequency (see the Supporting Information for detailed matrix representations and calculations). Therefore, the SHG signal of crystals with $\theta_{\text{co}} = 0^\circ$ is polarized parallel to the excitation polarization (ω), and these crystals are clearly observed in $p_{\text{in}}p_{\text{out}}$ configuration, as shown in Figure 4b. In contrast, crystals with $\theta_{\text{co}} = 90^\circ$ (C2 of Figure 4b,c) are seen most clearly in $p_{\text{in}}s_{\text{out}}$ configuration (Figure 4c) because the induced SHG polarization is given by $\mathbf{P}_y(2\omega) = -2\epsilon_0\chi_{yxx}^{(2)}\mathbf{E}_x(\omega)^2$. This polarization dependence on crystallographic orientation is also confirmed in far-field SHG anisotropy measured with a rotating analyzer (Figure 4e).

Only $\mathbf{E}_x(\omega)$ contributes to the SHG signal in the $p_{\text{in}}s_{\text{out}}$ configuration. Therefore, with $I_{2\omega} \propto |\mathbf{P}(2\omega)|^2 \propto |\mathbf{E}(\omega)|^4$, we can calculate the enhanced SHG intensity using the 35° tilted tip ($\mathbf{I}_{2\omega, \text{MoS}_2}^{35^\circ}$) compared to the conventional surface-normal-oriented tip ($\mathbf{I}_{2\omega, \text{MoS}_2}^{90^\circ}$) from the FDTD simulation. As shown in Figure 4d, the spatially integrated $|\mathbf{E}_x(\omega)|^4$ for the 35° tilted tip at the sample plane is ~ 28 times larger than that of the surface-normal oriented tip ($\theta_{\text{tip}} = 90^\circ$), i.e., $\mathbf{I}_{2\omega, \text{MoS}_2}^{35^\circ} / \mathbf{I}_{2\omega, \text{MoS}_2}^{90^\circ} \approx 28$.

Figure 4f shows a measured tip-enhanced nano-SHG image in $p_{\text{in}}s_{\text{out}}$ configuration for a small area selected within the far-field image. Far-field images of p_{out} and s_{out} detection are magnified in panels g and h of Figure 4 for comparison. As demonstrated previously,^{6,42} some GBs are visualized in the far-field SHG images due to the constructive (or destructive) interference between the SHG signals of adjacent crystals. However, this interference contrast at GBs is observed only for specific crystal orientations or polarization conditions.⁴²

In contrast, in the tip-enhanced SHG image (Figure 4f), a full GB map is obtained with pronounced SHG contrast. For example, while GB2 is observed in both far- and near-field images, the additional GBs (GB1, GB3, and GB4) are only seen in the near-field image. In contrast to the far-field response, a full GB map can be obtained regardless of crystal orientation and interference. Note that the near-field SHG signal at GBs emerges predominantly from the quasi 1D region confined near the GB. Thus, the detected near-field SHG signal at GB is weaker than that of crystal face due to the modified nonlinear optical susceptibility and broken symmetry at the defect.

To assess the full benefit of increased both in-plane and out-of-plane field confinement (Figure 2d), we then perform tip-enhanced nano-SHG imaging on single-crystalline x -cut YMnO_3 , as a model system of 6 mm point group with both in-plane and out-of-plane nonlinear optical susceptibility.^{34,35} We first deduce the microscopic sample orientation from far-field SHG anisotropy measurement as shown in Figure 5a. Based on this information, we probe the ferroelectric $\chi_{zxx}^{(2)} = \chi_{zyy}^{(2)}$ tensor elements in $p_{\text{in}}s_{\text{out}}$ tip-enhanced near-field microscopy configuration. The corresponding SHG polarization is then given by $\mathbf{P}_z(2\omega) = 2\epsilon_0\chi_{zxx}^{(2)}(\mathbf{E}_x(\omega)^2 + \mathbf{E}_y(\omega)^2)$ (see the Supporting Information for detailed matrix representations and calculations). The measured intensity $I_{2\omega}$ is proportional to $|\mathbf{E}_x(\omega)^2 + \mathbf{E}_y(\omega)^2|^2 = |\mathbf{E}_x(\omega)|^4 + |\mathbf{E}_y(\omega)|^4 + 2|\mathbf{E}_x(\omega)|^2|\mathbf{E}_y(\omega)|^2$. From the spatially integrated $|\mathbf{E}_x(\omega)|^4$, $|\mathbf{E}_y(\omega)|^4$, $|\mathbf{E}_x(\omega)|^2$, and $|\mathbf{E}_y(\omega)|^2$ values at the sample plane for the 35° tilted and surface-normal oriented tips (Figure 5b), we can estimate the tip-enhanced SHG intensity ratio of $\mathbf{I}_{2\omega, \text{YMnO}_3}^{35^\circ} / \mathbf{I}_{2\omega, \text{YMnO}_3}^{90^\circ} \sim 27$.

Panels c and d of Figure 5 show the resulting tip-enhanced SHG images under tilted tip ($\theta_{\text{tip}} = 35^\circ$) and surface-normal tip ($\theta_{\text{tip}} = 90^\circ$) configuration. We observe a high-contrast image of the domains with only the tilted tip. The details of contrast are due to the interference between the tip-enhanced SHG from a single domain and residual far-field SHG from multiple domains giving rise to a local phase-sensitive signal.³⁵ From that image, we can obtain the corresponding ferroelectric domain map exhibiting an alternating ferroelectric polarization pattern as expected for this crystallographic orientation (Figure 5e). In addition, we observe the 3-fold symmetric vortices of the domains (red boxes) as expected for hexagonal manganites,^{43,44} which provide information for the understanding of topological behaviors of ferroics.

In summary, a conventional surface-normal oriented tip geometry in tip-enhanced near-field microscopy gives limited polarization control in both the intrinsic far-field excitation and the extrinsic near-field nano-optical response. Furthermore, for surface-normal tip orientation, the antenna mode driven into a semi-infinite tip structure results in reduced field enhancement due to overdamping, which gives rise to reduced efficiency for both in-plane and out-of-plane nano-optical response. Our work presents a simple but powerful solution to control the vector-field of a nano-optical antenna-tip. We show that the optical field confinement can be systematically controlled by tuning the tip orientation angle with respect to the sample surface to enhance the in-plane optical field (\mathbf{E}_x) confinement for vector-field nano-imaging. Surprisingly, rather than an associated decrease in out-of-plane sensitivity with increasing tilt angle, the out-of-plane optical field (\mathbf{E}_z) is also enhanced with an even larger enhancement factor than \mathbf{E}_x . We find that at an optimized angle near 35° with details depending on tip material, sample, and excitation wavelength, the broken axial symmetry provides for a more-sensitive nanoprobe beyond conventional near-field microscopy tip for all optical modalities and any sample. The vector-field controllability of plasmonic antenna tips allows the probing of selective polarization components of samples by simply changing its tilting angle; in addition, this strongly confined vector-field gives access to enhanced nanoscale light-matter interactions such as exciton-plasmon coupling,⁴⁵ electron-phonon coupling,⁴⁶ and strong coupling⁴⁷ in a range of photoactive molecules and quantum materials.

■ ASSOCIATED CONTENT

Supporting Information

The Supporting Information is available free of charge on the ACS Publications website at DOI: 10.1021/acs.nanolett.8b00108.

Figures showing the etched Au tip, simulated electric-field intensity maps, simulated optical-field intensity profiles, AFM topography, an AFM phase, and tip-enhanced SHG nano-crystallography results. Additional details on selection rules. (PDF)

■ AUTHOR INFORMATION

Corresponding Author

*E-mail: markus.raschke@colorado.edu. Phone: (+1)-303-4921366.

ORCID

Kyoung-Duck Park: 0000-0002-9302-9384

Markus B. Raschke: 0000-0003-2822-851X

Author Contributions

M.B.R. and K.-D.P. conceived the experiment. K.-D.P. performed the measurements and the FDTD simulations. K.-D.P. and M.B.R. analyzed the data and discussed the results. K.-D.P. and M.B.R. wrote the manuscript. M.B.R. supervised the project.

Notes

The authors declare no competing financial interest.

ACKNOWLEDGMENTS

The authors thank Joanna M. Atkin for insightful discussions. We thank Xiaobo Yin and Manfred Fiebig for providing the MoS₂ and the YMnO₃ samples, respectively. We acknowledge funding from the U.S. Department of Energy, Office of Basic Sciences, Division of Material Sciences and Engineering, under award no. DE-SC0008807. We also acknowledge support provided by the Center for Experiments on Quantum Materials (CEQM) of the University of Colorado.

REFERENCES

- (1) Midwinter, J.; Warner, J. *Br. J. Appl. Phys.* **1965**, *16*, 1135–1142.
- (2) Berweger, S.; Raschke, M. B. *J. Raman Spectrosc.* **2009**, *40*, 1413–1419.
- (3) Anastassakis, E. *J. Appl. Phys.* **1997**, *82*, 1582–1591.
- (4) Fiebig, M.; Fröhlich, D.; Kohn, K.; Lottermoser, T.; Pavlov, V.; Pisarev, R.; Leute, S. *Phys. Rev. Lett.* **2000**, *84*, 5620–5623.
- (5) Najafov, H.; Lee, B.; Zhou, Q.; Feldman, L.; Podzorov, V. *Nat. Mater.* **2010**, *9*, 938–943.
- (6) Yin, X.; Ye, Z.; Chenet, D. A.; Ye, Y.; O'Brien, K.; Hone, J. C.; Zhang, X. *Science* **2014**, *344*, 488–490.
- (7) Gerton, J. M.; Wade, L. A.; Lessard, G. A.; Ma, Z.; Quake, S. R. *Phys. Rev. Lett.* **2004**, *93*, 180801.
- (8) Yano, T.-a.; Verma, P.; Saito, Y.; Ichimura, T.; Kawata, S. *Nat. Photonics* **2009**, *3*, 473–477.
- (9) Zhang, R.; Zhang, Y.; Dong, Z.; Jiang, S.; Zhang, C.; Chen, L.; Zhang, L.; Liao, Y.; Aizpurua, J.; Luo, Y.; Yang, J.; Hou, J. *Nature* **2013**, *498*, 82–86.
- (10) Lee, K.; Kihm, H.; Kihm, J.; Choi, W.; Kim, H.; Ropers, C.; Park, D.; Yoon, Y.; Choi, S.; Woo, D.; Kim, J.; Lee, B.; Park, Q.; Lienau, C.; Kim, D. *Nat. Photonics* **2007**, *1*, 53–56.
- (11) Olmon, R. L.; Rang, M.; Krenz, P. M.; Lail, B. A.; Saraf, L. V.; Boreman, G. D.; Raschke, M. B. *Phys. Rev. Lett.* **2010**, *105*, 167403.
- (12) Burrelli, M.; Van Oosten, D.; Kampfrath, T.; Schoenmaker, H.; Heideman, R.; Leinse, A.; Kuipers, L. *Science* **2009**, *326*, 550–553.
- (13) Kihm, H.; Koo, S.; Kim, Q.; Bao, K.; Kihm, J.; Bak, W.; Eah, S.; Lienau, C.; Kim, H.; Nordlander, P.; et al. *Nat. Commun.* **2011**, *2*, 451.
- (14) Gerber, J. A.; Berweger, S.; O'Callahan, B. T.; Raschke, M. B. *Phys. Rev. Lett.* **2014**, *113*, 055502.
- (15) Fei, Z.; Rodin, A.; Andreev, G.; Bao, W.; McLeod, A.; Wagner, M.; Zhang, L.; Zhao, Z.; Thiemens, M.; Dominguez, G.; et al. *Nature* **2012**, *487*, 82–85.
- (16) Chen, J.; Badioli, M.; Alonso-gonzález, P.; Thongrattanasiri, S.; Huth, F.; Osmond, J.; Spasenović, M.; Centeno, A.; Pesquera, A.; Godignon, P.; et al. *Nature* **2012**, *487*, 77–81.
- (17) Park, K.-D.; Khatib, O.; Kravtsov, V.; Clark, G.; Xu, X.; Raschke, M. B. *Nano Lett.* **2016**, *16*, 2621–2627.
- (18) Bao, W.; Borys, N. J.; Ko, C.; Suh, J.; Fan, W.; Thron, A.; Zhang, Y.; Buyanin, A.; Zhang, J.; Cabrini, S.; et al. *Nat. Commun.* **2015**, *6*, 8993.
- (19) Li, Z.; Xiao, Y.; Gong, Y.; Wang, Z.; Kang, Y.; Zu, S.; Ajayan, P. M.; Nordlander, P.; Fang, Z. *ACS Nano* **2015**, *9*, 10158–10164.
- (20) Damodaran, A.; Clarkson, J.; Hong, Z.; Liu, H.; Yadav, A.; Nelson, C.; Hsu, S.-L.; McCarter, M.; Park, K.-D.; Kravtsov, V.; et al. *Nat. Mater.* **2017**, *16*, 1003–1009.
- (21) Kalantar-zadeh, K.; Ou, J. Z.; Daeneke, T.; Mitchell, A.; Sasaki, T.; Fuhrer, M. S. *Appl. Mater. Today* **2016**, *5*, 73–89.
- (22) Kildishev, A. V.; Boltasseva, A.; Shalae, V. M. *Science* **2013**, *339*, 1232009.
- (23) Berweger, S.; Neacsu, C. C.; Mao, Y.; Zhou, H.; Wong, S. S.; Raschke, M. B. *Nat. Nanotechnol.* **2009**, *4*, 496–499.
- (24) Muller, E. A.; Pollard, B.; Bechtel, H. A.; van Blerkom, P.; Raschke, M. B. *Sci. Adv.* **2016**, *2*, e1601006.
- (25) Mino, T.; Saito, Y.; Verma, P. *ACS Nano* **2014**, *8*, 10187–10195.
- (26) Kharintsev, S. S.; Fishman, A. I.; Kazarian, S. G.; Salakhov, M. K. *Phys. Rev. B: Condens. Matter Mater. Phys.* **2015**, *92*, 115113.
- (27) Talley, C. E.; Jackson, J. B.; Oubre, C.; Grady, N. K.; Hollars, C. W.; Lane, S. M.; Huser, T. R.; Nordlander, P.; Halas, N. J. *Nano Lett.* **2005**, *5*, 1569–1574.
- (28) Sanders, A.; Bowman, R. W.; Zhang, L.; Turek, V.; Sigle, D. O.; Lombardi, A.; Weller, L.; Baumberg, J. J. *Appl. Phys. Lett.* **2016**, *109*, 153110.
- (29) Maximiano, R. V.; Beams, R.; Novotny, L.; Jorio, A.; Cançado, L. G. *Phys. Rev. B: Condens. Matter Mater. Phys.* **2012**, *85*, 235434.
- (30) Kharintsev, S.; Rogov, A.; Kazarian, S. *Rev. Sci. Instrum.* **2013**, *84*, 093106.
- (31) Kumar, N.; Najmaei, S.; Cui, Q.; Ceballos, F.; Ajayan, P. M.; Lou, J.; Zhao, H. *Phys. Rev. B: Condens. Matter Mater. Phys.* **2013**, *87*, 161403.
- (32) Seyler, K. L.; Schaibley, J. R.; Gong, P.; Rivera, P.; Jones, A. M.; Wu, S.; Yan, J.; Mandrus, D. G.; Yao, W.; Xu, X. *Nat. Nanotechnol.* **2015**, *10*, 407–411.
- (33) Hsu, W.-T.; Zhao, Z.-A.; Li, L.-J.; Chen, C.-H.; Chiu, M.-H.; Chang, P.-S.; Chou, Y.-C.; Chang, W.-H. *ACS Nano* **2014**, *8*, 2951–2958.
- (34) Fiebig, M.; Fröhlich, D.; Lottermoser, T.; Maat, M. *Phys. Rev. B: Condens. Matter Mater. Phys.* **2002**, *66*, 144102.
- (35) Neacsu, C. C.; van Aken, B. B.; Fiebig, M.; Raschke, M. B. *Phys. Rev. B: Condens. Matter Mater. Phys.* **2009**, *79*, 100107.
- (36) Stadler, J.; Schmid, T.; Zenobi, R. *Nano Lett.* **2010**, *10*, 4514–4520.
- (37) Chan, K. A.; Kazarian, S. G. *Nanotechnology* **2011**, *22*, 175701.
- (38) Nottingher, I.; Elfick, A. J. *J. Phys. Chem. B* **2005**, *109*, 15699–15706.
- (39) Grigorchuk, N. I. *J. Opt. Soc. Am. B* **2012**, *29*, 3404–3411.
- (40) Malard, L. M.; Alencar, T. V.; Barboza, A. P. M.; Mak, K. F.; de Paula, A. M. *Phys. Rev. B: Condens. Matter Mater. Phys.* **2013**, *87*, 201401.
- (41) Li, Y.; Rao, Y.; Mak, K. F.; You, Y.; Wang, S.; Dean, C. R.; Heinz, T. F. *Nano Lett.* **2013**, *13*, 3329–3333.
- (42) Cheng, J.; Jiang, T.; Ji, Q.; Zhang, Y.; Li, Z.; Shan, Y.; Zhang, Y.; Gong, X.; Liu, W.; Wu, S. *Adv. Mater.* **2015**, *27*, 4069–4074.
- (43) Chae, S.; Lee, N.; Horibe, Y.; Tanimura, M.; Mori, S.; Gao, B.; Carr, S.; Cheong, S.-W. *Phys. Rev. Lett.* **2012**, *108*, 167603.
- (44) Jungk, T.; Hoffmann, Á.; Fiebig, M.; Soergel, E. *Appl. Phys. Lett.* **2010**, *97*, 012904.
- (45) Park, K.-D.; Jiang, T.; Clark, G.; Xu, X.; Raschke, M. B. *Nat. Nanotechnol.* **2018**, *13*, 59–64.
- (46) Jin, C.; Kim, J.; Suh, J.; Shi, Z.; Chen, B.; Fan, X.; Kam, M.; Watanabe, K.; Taniguchi, T.; Tongay, S.; Zettl, A.; Wu, J.; Wang, F. *Nat. Phys.* **2017**, *13*, 127–131.
- (47) Chikkaraddy, R.; de Nijs, B.; Benz, F.; Barrow, S. J.; Scherman, O. A.; Rosta, E.; Demetriadou, A.; Fox, P.; Hess, O.; Baumberg, J. J. *Nature* **2016**, *535*, 127–130.